The Effects of Late Cenozoic Climate Change on the Global Distribution of Frost Cracking

Hemanti Sharma[1], Sebastian G. Mutz[1], Todd A. Ehlers[1*]

[1]Department of Geosciences, University of Tuebingen, Tuebingen, 72076, Germany

*Correspondence to: Todd A. Ehlers (todd.ehlers@uni-tuebingen.de)

Abstract. Frost cracking is a dominant mechanical weathering phenomenon facilitating the breakdown of bedrock in periglacial regions. Despite recent advances in understanding frost cracking processes, few studies have addressed how global climate change over the Late Cenozoic may have impacted spatial variations in frost cracking intensity. In this study, we estimate global changes in frost cracking intensity (FCI) by segregation ice growth. Existing process-based models of FCI are applied in combination with soil thickness data from the Harmonized World Soil Database. Temporal and spatial variations in FCI are predicted using surface temperatures changes obtained from ECHAM5 general circulation model simulations conducted for four different paleoclimate time-slices. Time-slices considered include Pre-Industrial (~1850 CE, PI), Mid-Holocene (~6 ka, MH), Last Glacial Maximum (~21 ka, LGM) and Pliocene (~3 Ma, PLIO) times. Results indicate for all paleoclimate time slices that frost cracking was most prevalent (relative to PI times) in the mid to high latitude regions, as well as high-elevation lower latitudes areas such the Himalayas, Tibet, European Alps, the Japanese Alps, the USA Rocky Mountains, and the Andes Mountains. The smallest deviations in frost cracking (relative to PI conditions) were observed in the MH simulation, which yielded slightly higher FCI values in most of the areas. In contrast, larger deviations were observed in the simulations of the colder climate (LGM) and warmer climate (PLIO). Our results indicate that the impact of climate change on frost cracking was most severe during the PI – LGM period due to higher differences in temperatures and glaciation at higher latitudes. In contrast, the PLIO results indicate low FCI in the Andes and higher values of FCI in Greenland and Canada due to the diminished extent of glaciation in the warmer PLIO climate.

Keywords: Climate Change, frost cracking, physical weathering, Pre-Industrial, Mid-Holocene, Last Glacial Maximum, Pliocene

1. Introduction

Climate change, mountain building, and erosion are closely linked over different spatial and temporal scales (e.g. Whipple, 2009; Adams et al., 2020). Over long (million year) timescales, mountain building alters global climate by introducing physical obstacles to atmospheric flow (Raymo and Ruddiman, 1992) that influences regional temperatures and precipitation (Botsyun et al., 2020; Ehlers and Poulsen, 2009; Mutz et al., 2018; Mutz and Ehlers, 2019). Over decadal to million-year time scales, climate change impacts the erosion of mountains both indirectly, e.g. through the modification of vegetation cover (e.g. Acosta et al., 2015; Schmid et al., 2018; Werner et al., 2018; Starke et al., 2020), and directly through its influence on physical and chemical weathering processes, as well as glacial, fluvial and hillslope erosion (e.g. Valla et al., 2011; Herman et al., 2013; Lease and Ehlers, 2013; Perron, 2017). Climate change from the Late Cenozoic to present has played an important role in eroding mountain topography and lowland sedimentation (Hasler et al., 2011; Herman and Champagnac, 2016; Marshall et al., 2015; Peizhen et al., 2001; Rangwala and Miller, 2012). Climate change influences surface processes through not only precipitation changes, but also through seasonal temperature changes that affect physical weathering mechanisms, such as frost cracking (Anderson, 1998; Delunel et al., 2010; Hales and Roering, 2007; Walder and Hallet, 1985). Frost cracking occurs

37 when the pressure of freezing (and expanding) water in pore walls or fractures exceeds the cohesive strength of the porous

38 media and causes cracks to propagate (Davidson and Nye, 1985). Frost cracking is a dominant mechanism of weathering in

39 periglacial regions (Marshall et al., 2015), and typically occurs at latitudes greater than 30°N and 30°S. Here, we complement

40 previous work on the effects of climate on surface processes by addressing the following hypothesis: If Late Cenozoic global

41 climate change resulted in latitudinal variations in ground surface temperatures, then the intensity of frost cracking should

42 temporally and spatially vary in such a way that leads to the occurrence of more intense frost cracking at lower latitudes during

43 colder climates.

44 Previous field studies of frost cracking in mountain regions includes studies in, for example, the Japanese Alps (Matsuoka,

45 2001), Southern Alps of New Zealand (Hales and Roering, 2009), Swiss Alps (Amitrano et al., 2012; Girard et al., 2013;

46 Matsuoka, 2008; Messenzehl et al., 2017), French Western Alps (Delunel et al., 2010), Italian Alps (Savi et al., 2015), Eastern

47 Alps (Rode et al., 2016), Austrian Alps (Kellerer-Pirklbauer, 2017), Oregon (Marshall et al., 2015; Rempel et al., 2016), and

48 the Rocky Mountains, USA (Anderson, 1998). These studies demonstrated clear relationships between changes in near surface

49 air temperatures and frost cracking. Various process-based models have also been developed to estimate frost cracking

50 intensity (FCI) using mean annual air temperatures (MAT) (Andersen et al., 2015; Anderson, 1998; Anderson et al., 2013;

51 Hales and Roering, 2007; Marshall et al., 2015) and in some cases, with the additional consideration of sediment thickness

52 variations over bedrock (Andersen et al., 2015). These studies document the importance of time spent in the frost-cracking

53 window for the frost-cracking intensity (FCI) of a given area. The frost-cracking window is based on the premise that cracking

54 occurs in response to segregation ice growth in bedrock when subsurface temperatures are between -8 °C and -3 °C (Anderson,

55 1998; Walder and Hallet, 1985). More complex models consider near surface thermal gradients as a proxy of the frost cracking

56 intensity for segregation ice growth, as well as the effects of overlying sediment layer thickness on frost cracking (Andersen

57 et al., 2015).

58 The previous studies provide insight into not only observed regional variations in frost cracking, but also some of the key

59 processes required for predicting frost cracking intensity. However, despite recognition that Late Cenozoic global climate

60 change impacts surface processes (e.g., Mutz et al., 2018; Mutz and Ehlers, 2019) and frost-cracking intensity (e.g. Marshall

61 et al., 2015), to the best of our knowledge, no study has taken full advantage of climate change predictions in conjunction with

62 a process-based understanding of the spatiotemporal variations in frost cracking on a global scale. This study builds upon

63 previous work by estimating the global response in FCI to different end-member climate states. We do this by coupling existing

64 frost-cracking models to high-resolution paleoclimate General Circulation Model (GCM) simulations (Mutz et al., 2018). More

65 specifically we apply three different frost-cracking models that are driven by predicted surface temperature changes from GCM

66 time-slice experiments including (a) the Pliocene (~3 Ma, PLIO), considered an analog for Earth's potential future due to

67 anthropogenic climate change, (b) the Last Glacial Maximum (~21 ka, LGM), covering a full glacial period, (c) the Mid-

68 Holocene (~6 ka, MH) climate optimum, and (d) Pre-Industrial (~1850 CE, PI) conditions before the onset of significant

69 anthropogenic disturbances to climate. In addition to a global analysis, we investigate how FCI varies for selected orogens

70 including the Himalaya-Tibet, Europe and the Andes.

71 **2. Data**

72 This manuscript builds upon paleoclimate model simulations we previously published for different time periods (Mutz et al.,

73 2018; Mutz and Ehlers, 2019). The output from those simulations was used for new calculations of FCI described below.

74 More specifically, the climate and soil used for this study includes simulated daily land surface temperatures from different

75 paleoclimatic time-slice experiments (PI, MH, LGM and PLIO) conducted with the GCM ECHAM5 simulations (Mutz et al.,

76   2018), and soil thickness data (Wieder, 2014). Due to the lack of paleo soil thickness data, global variations in soil thickness

77   are assumed to be uniform between all time-slices investigated.

78   The ECHAM5 paleoclimate simulations have a high spatial resolution (T159, corresponding roughly to a 80km x 80km

79   horizontal grid at the equator) and 31 vertical levels (to 10hPa). ECHAM5 was developed at the Max Planck Institute for

80   Meteorology (Roeckner et al., 2003). It is based on the spectral weather forecast model of ECMWF (Simmons et al., 1989)

81   and is a well-established tool in modern and paleoclimate studies. The ECHAM5 paleoclimate simulations by Mutz et al.

82   (2018) were driven with time-slice specific boundary conditions derived from multiple modeling initiatives and

83   paleogeographic, paleoenvironmental and vegetation reconstruction projects. (see Table 1). Details about the boundary

84   conditions and prevailing climates for specific time-slices (PI, MH, LGM and PLIO) are provided in Mutz et al. (2018). Each

85   simulated time-slice resulted in 17 simulated model years, where the first two years contained model spin up effects and were

86   discarded. The remaining 15 years of simulated climate were in dynamic equilibrium with the prescribed boundary conditions

87   and used for our analysis.

88

89   **Table 1. Boundary Conditions of the paleoclimate simulations *(Mutz et al., 2018)*.**

Paleoclimate Simulations	Boundary Conditions
PI (~ 1850)	• Sea-Surface temperatures (SST) and sea-ice concentrations (SIC) were sourced from transient coupled ocean-atmosphere simulations (Dietrich et al., 2013; Lorenz and Lohmann, 2004) • Green-house gas (GHG) concentrations (Dietrich et al., 2013) were obtained from ice-core-based reconstructions of CO_2 (Etheridge et al., 1996), CH_2 (Etheridge et al., 1998), and N_2O (Sowers et al., 2003)
MH (~ 6 ka)	• SST and SIC are derived from a transient, low resolution, coupled atmosphere-ocean simulation of the mid (6 ka) Holocene (Lohmann et al., 2013; Wei and Lohmann, 2012) • GHG concentrations (Dietrich et al., 2013) are obtained from ice-core-based reconstructions of CO_2 (Etheridge et al., 1996), CH_2 (Etheridge et al., 1998), and N_2O (Sowers et al., 2003) • Global vegetation maps are based on plant functional types maps by the BIOME 6000 / Palaeovegetation Mapping Project (Prentice et al., 2000; Harrison et al., 2001; Bigelow et al., 2003; Pickett et al., 2004) and model predictions by Arnold et al. (2009) • Orbital parameters from Dietrich et al., (2013)
LGM (~ 21 ka)	• Land-sea distribution and ice sheet extent and thickness are based on the PMIP III guidelines (Abe-Ouchi et al., 2015) • SST and SIC are based on GLAMAP (Sarnthein et al, 2003) and CLIMAP (CLIMAP group members, 1981) reconstructions • GHGs concentrations are prescribed following Otto-Bliesner et al. (2006) • Global vegetation maps are based on the plant functional types maps by the BIOME 6000 / Palaeovegetation Mapping Project (Prentice et al., 2000; Harrison et al., 2001; Bigelow et al., 2003; Pickett et al., 2004) and model predictions by Arnold et al. (2009) • Orbital parameters from Dietrich et al., (2013)
PLIO (~ 3 Ma)	• Surface conditions (SST, SIC, sea land mask, topography and ice cover), GHG concentrations and orbital parameters are obtained from the PRISM project (Haywood et al., 2010; Sohl et al., 2009; Dowsett et al., 2010) • PRISM vegetation reconstruction converted to ECHAM5 compatible plant functional types following Stepanek and Lohmann (2012)

90

91 *(SST: Sea Surface Temperature; SIC: Sea Ice Concentration; GHG: Greenhouse Gas; PMIP III: Paleoclimate Modelling

92 *Intercomparison Project, phase 3; PRISM: Pliocene Research, Interpretation and Synoptic Mapping)*

Soil Depth [cm] (Harmonised World Soil Database (version 1.2))
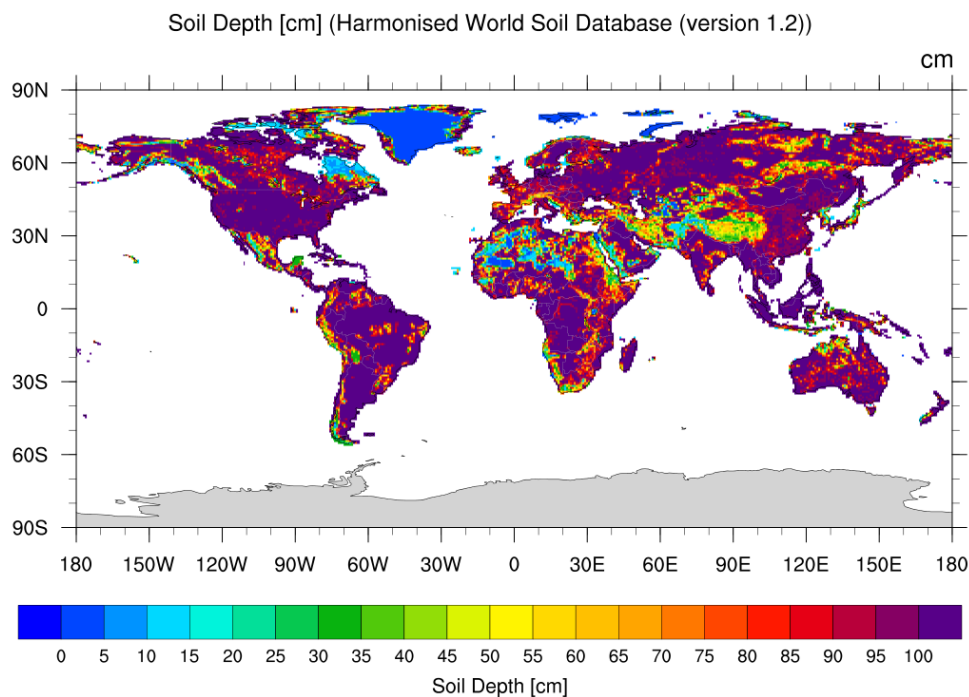
93

94 **Figure 1. Soil depth map from the Harmonized World Soil Databased (HWSD, version 1.2) used in this study (Wieder, 2014).**

95 Soil thickness data was obtained from the re-gridded Harmonized World Soil Database (HWSD) v1.2 (Wieder, 2014) which

96 has a 0.05-degree spatial resolution and depths ranging from 0 m to 1 m (Fig. 1). In the dataset, reference soil depth for all the

97 soil units is set to 100 cm, except for Rendzinas and Rankers of FAO-74 and Leptosols of FAO-90, where the reference soil

98 depth is set to 30 cm, and Lithosols of FAO-74 and Lithic Leptosols of FAO-90, where it is set to 10 cm (Wieder, 2014). The

99 above soil thickness data was upscaled to match the spatial resolution of the ECHAM5 paleoclimate simulations (T159, ca.

100 80km x 80km).

101 **3. Methods**
102 **3.1. Pre-processing of GCM simulation temperature data**

103 We calculated the mean annual land surface temperatures (MAT) to serve as input for subsequent calculations and a reference

104 for differences in global paleoclimate. The MAT's for the paleoclimate GCM experiments (PLIO, LGM, MH, and PI) were

105 calculated (Fig. 2) from each of the simulations' 15 years of daily land surface temperature values. In addition, the half

106 amplitude of annual surface temperature variations (Ta) was extracted at all surface grid locations for all years (Fig. 3). We

107 use the MAT for ground surface temperature in subsequent calculations, following Anderson et al., (2013), Marshall et al.,

108   (2015), and Rempel et al., (2016)) . The maxima and minima for global average MAT's and Ta's for all the time-slices are

109   shown in Table 2.
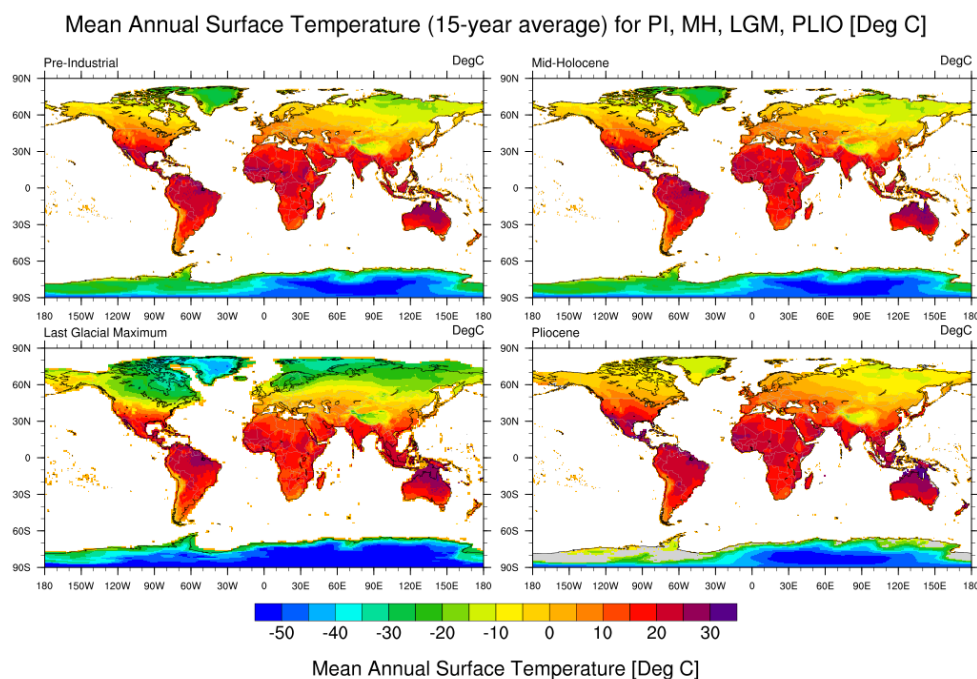
110

111   **Figure 2. Mean Annual Surface Temperature maps (15-year average) from the ECHAM5 GCM simulations for the Pre-Industrial**

112   **(top-left), Mid-Holocene (top-right), Last Glacial Maximum (bottom-left), and mid-Pliocene (bottom-right) (unit: °C). These are**

113   **calculated from GCM simulation output of Mutz et al. (2018) and Mutz and Ehlers (2019).**

114   **Table 2. MAT and Ta (for ground surface temperature) for Pre-Industrial, Mid-Holocene, Last Glacial Maximum and Pliocene**

115   **simulations.**

Time-slices (Paleoclimate Simulations)	MAT (°C)		Ta (°C)	
	Minimum	**Maximum**	**Minimum**	**Maximum**
Pre-Industrial (~ 1850)	-58.31	34.03	0	38.64
Mid-Holocene (~ 6 ka)	-58.50	35.19	0	39.6
Last Glacial Maximum (~21 ka)	-66.93	38.74	0	41.74
Pliocene (~ 3 Ma)	-56.20	48.23	0	43.21

116

117   The calculation of temporally varying sub-surface temperatures follows the approach of Hales and Roering (2007) and uses

118   the analytical solution for the one-dimensional heat conduction equation (Turcotte and Schubert, 2014) forced with daily

119   temperatures following sinusoidal variations. Temperature variations with depth and time can were calculated at each GCM

120   grid point as:

121    $$T(z,t) = MAT + Ta \cdot e^{-z\sqrt{\frac{\pi}{\alpha P_y}}} \cdot sin\left(\frac{2\pi t}{P_y} - z\sqrt{\frac{\pi}{\alpha P_y}}\right) \qquad (1)$$

122   where, T represents daily subsurface temperature at depth z (m) and time t (days in a year), MAT and Ta represent mean annual

123   surface temperature and half amplitude of annual temperature variation respectively, P_y is the period of the sinusoidal cycle (1

124   year), and α is the thermal diffusivity. Thermal diffusivity values near the Earth's surface can range from $1 - 2 \times 10^{-6} m^2 s^{-1}$

125   for most rocks (Anderson, 1998) and range between $7 - 10 \times 10^{-7} m^2 s^{-1}$ for other Earth materials comprising the overlying

126   sediment layer (Eppelbaum et al., 2014). In this study, we used a thermal diffusivity of $1.5 \times 10^{-6} m^2 s^{-1}$ for bedrock and $8 \times$

127   $10^{-7} m^2 s^{-1}$ for the overlying sediment layer. The maximum depth investigated here is 20 m, as it is slightly deeper than the

128   maximum frost penetration depth of ~14 m reported by (Hales and Roering, 2007).

129
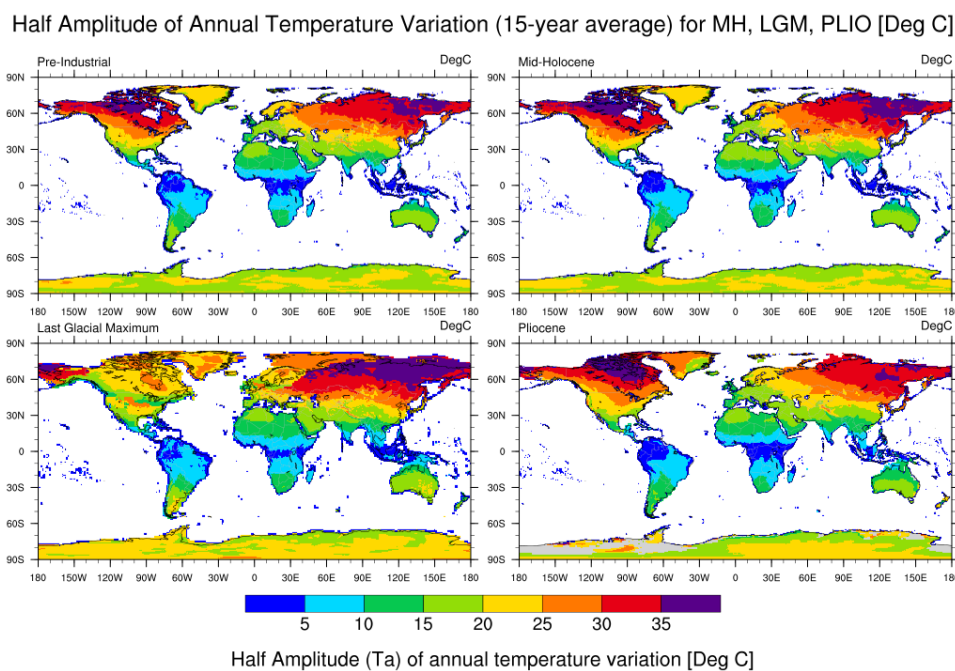
Figure 3. Half Amplitude of Annual Temperature Variation (15-year average) for the Pre-Industrial (top-left), Mid-Holocene (top-right), Last Glacial Maximum (bottom-left), and Pliocene (bottom-right) (unit: °C). These are calculated from GCM simulation output of Mutz et al., (2018) and Mutz and Ehlers (2019).

133   The calculation of subsurface temperatures was discretized into 200 depth intervals from the surface to the maximum depth of

134   20 m. Smaller depth intervals (~1 cm) were used near the surface and large intervals (~20 cm) at greater depths, because the

135   FCI is expected to change most dramatically near the surface and dampen with depth due to thermal diffusion (Andersen et

136   al., 2015).

3.2.   Estimation of Frost Cracking Intensity

138   We applied three different approaches (models) with different levels of complexity to estimate global variations in frost

139   cracking during different past climates (Fig 4; Andersen et al., 2015; Anderson, 1998; Hales and Roering, 2007). The models

140   use predicted ground surface temperatures from each grid cell in the GCM to calculate subsurface temperatures and FCI. We

141   then calculate differences between the FCI from the PI reference simulation and the FCI predicted for the PLIO, LGM and

142   MH time-slices to assess relative change in FCI over the Late Cenozoic. The conceptual diagram (Fig. 4) illustrates differences

143   in the models used in our study, which are discussed in detail in sections 3.2.1 - 3.2.3. Models 1-3 successively increase in

144   complexity and consider more factors. The approach of Andersen et al., (2015), referred to here as Model 3, is the most recent

145   and complete in its consideration of the processes (e.g. effect of soil-cover on FCI) that are relevant for frost cracking. Given

146   this, we focus our presentation of results in the main text here on Model 3, but for completeness describe below differences of

147   Model 3 from earlier Models (1-2). For brevity, results from the earlier models are presented in the supplementary material. A

148   flowchart illustrating our methods is presented in Fig. 5. Similar to previous studies, the hydrogeological properties of the

149   bedrock (i.e. infiltration, water saturation, porosity and permeability) are ignored in this study. This approach provides a

150   simplified means for estimating the FCI for underlying bedrock at a global scale.

151
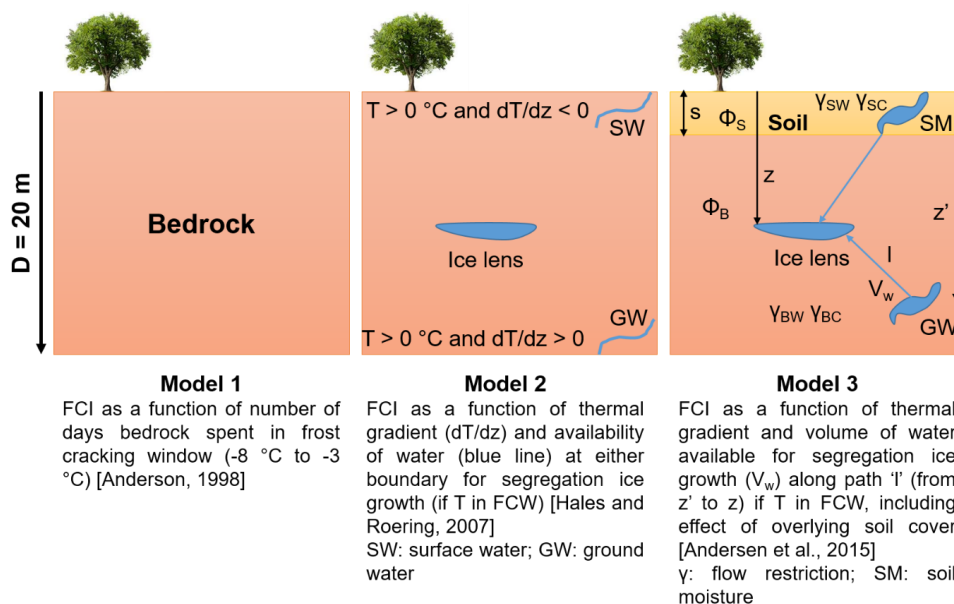
152

153   **Figure 4. Conceptual diagram of the models (1, 2, and 3) used for estimating FCI (T: temperature; dT/dz: thermal gradient; SW:**

154   **surface water; GW: groundwater; SM: soil moisture; s: sediment thickness; φS: soil porosity (0.02); φB: bedrock porosity (0.3)).**

155
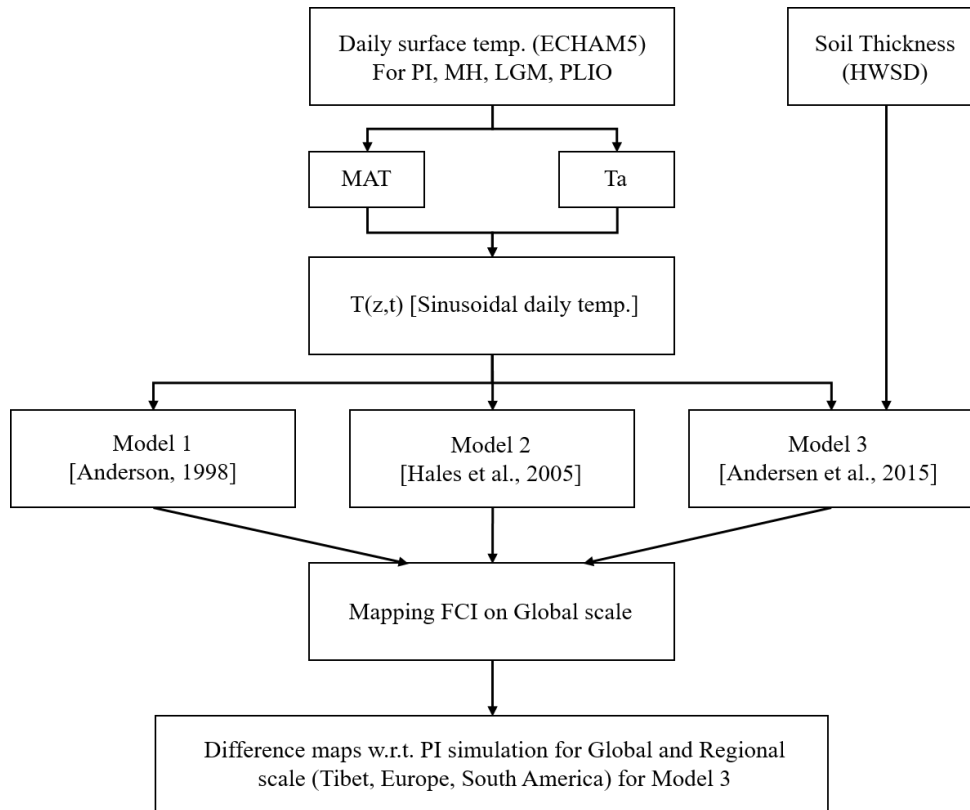
Figure 5. Flowchart describing the methods used in the study based on daily surface temperature simulated by the ECHAM GCM.

and soil thickness data from HWSD v1.2. Abbreviations include: MAT - mean annual temperature; Ta - half amplitude of annual

temperature variation; T (z, t) - subsurface temperature at depth z and time t; FCI - frost cracking intensity.

3.2.1.   Model 1: Frost cracking intensity as a function of time spent in the frost cracking window (FCW)

Model 1 represents the simplest approach and applies the method of Anderson (1998). In our application of this model we use

a more representative thermal diffusivity value for rocks of $1.5 \times 10^{-7} m^2 s^{-1}$, because the previous study was specific to

granitic bedrock and applied a diffusivity specific to that. Furthermore, the boundary conditions of a low rock surface albedo

(≤ 0.1) and presence of a high atmospheric transmissivity (≥ 0.9) on the surface were relaxed, as surface temperatures were

used in our study instead of near-surface air temperatures.

For our implementation of model 1, we applied equation 1 for sinusoidal varying daily temperatures at the surface, and

calculated temperatures up to 20 m depth. The number of days spent in the frost cracking window (-8 °C to - 3 °C) for each

depth interval were calculated over a period of 1 year for all time slices (PI, MH, LGM and PLIO):

$$FCI(z) = \begin{cases} N(z), if -8°C < T(z,t) - 3°C \\ 0, else \end{cases} \qquad (2)$$

where *FCI (z)* is referred to the frost cracking intensity at depth *z*. *N (z)* indicates the number of days the bedrock (at depth z)

spends in the frost cracking window over a period of 1 year.

Estimation of frost cracking intensity for each location included depth averaging of the FCI such that:

172    $\acute{FCI} = \frac{1}{D}\int_0^D FCI(z)dz$ (3)

173   where $\acute{FCI}$ is the integrated frost cracking intensity to a depth of $D = 20\ m$. The unit of integrated frost cracking intensity in

174   this model is $Days$. The FCI values are calculated for all model years separately and then averaged over the total time (15

175   years) for each paleoclimate time-slice.

3.2.2.   Model 2: Frost cracking intensity as a function of subsurface thermal gradients

177   Model 2 applies the approach of Hales and Roering (2007) to estimate FCI using climate change driven variations in subsurface

178   thermal gradients. This approach extends the work of Anderson (1998) with the additional consideration of segregation ice

179   growth. Segregated ice growth is attributed to the migration of liquid water to colder regions in shallow bedrock, accumulating

180   in localized zones to form ice lenses inducing weathering (Walder and Hallet, 1985).

181   For this approach, we applied equation 1 for temperatures to 20 m depth and for a time duration of 1 year. Again, FCI is

182   computed for each of the 15 years in the GCM simulation and averaged. To facilitate ice segregation growth, the model

183   assumes the availability of liquid water (T > 0 °C) at either boundary (z = 0 m or z = 20 m), with a negative thermal gradient

184   for a positive surface temperature, and a positive thermal gradient for the positive lower boundary (z = 20 m) temperature.

185   This implementation supports frost cracking in the bedrock with temperatures between – 8 °C and – 3 °C (Hallet et al., 1991).

186   In the case if permafrost areas, MAT is always negative, but as sinusoidal T (z, t) is calculated based on MAT and Ta, a positive

187   T (> 0 °C) may occur during warmer days of the year. In addition, Ta is higher for higher latitudes (Fig. 2), which are more

188   prone to frost cracking.

189   The model is described as follows:

190    $FCI(z,t) = \begin{cases} \left|\frac{dT}{dz}\right|(z,t), if -8°C < T(z,t) - 3°C \\ 0, else \end{cases}$ (4)

191    $\acute{FCI} = \int_0^D \int_0^{Py} FCI(z,t)dtdz$ (5)

192   where FCI (z, t) is the frost cracking intensity at depth z and time t. It is an index for the absolute value of the thermal gradient

193   at that particular depth and time that fulfils the conditions defined above.

194   In equation 5, $\acute{FCI}$ represents the integrated FCI for a geographic location. More specifically, the FCI is integrated over one

195   year at each depth and then integrated for all depth elements. D represents depth (20 m), Py is a period of the sinusoid (1 year),

196   dt is the time interval (1 day) and dz is the depth interval, as described in section 3.1. The unit of integrated frost cracking

197   intensity in this case is °C. It is calculated for each of the GCM model years and then averaged over the total time (15 years).

3.2.3.   Model 3: Frost cracking intensity as a function of thermal gradients and sediment thickness

199   In the final (most complex) approach used in this study, the effect of an overlying soil layer (Fig. 1) is considered in addition

200   to the subsurface thermal gradient variations with depth. This model applies the approach of Andersen et al. (2015), which

201   extends the work of Hales and Roering (2007) and Anderson et al. (2013). The model assumptions are similar to the previous

202   approaches. For segregation ice growth, it additionally takes into account the influence of the volume of water available in the

203   proximity of the ice lens. The parameters used in Model 3 are listed below (Table 3).

204 **Table 3.** Input parameters for Model 3 *(Andersen et al., 2015)*

Symbol	Description	Value
Φ_S	Porosity of soil	0.3
Φ_B	Porosity of bedrock	0.02
γ_{SW}	Flow restriction in warm soil	1.0 m^{-1}
γ_{SC}	Flow restriction in cold soil	2.0 m^{-1}
γ_{BW}	Flow restriction in warm bedrock	2.0 m^{-1}
γ_{BC}	Flow restriction in cold bedrock	4.0 m^{-1}
V_{CW}	Critical water volume	0.04 m

205

206   In Model 3, frost cracking intensity is estimated as a product of the thermal gradient and volume of water available (V_W) for

207   segregation ice growth at each depth element, such that:

208   $$FCI(z,t) = \begin{cases} \left|\frac{dT}{dz}(z,t)\right| V_W(z), & if -8°C < T(z,t) - 3°C \\ 0, & else \end{cases} \qquad (6)$$

209   where, *FCI (z, t)* is the frost cracking intensity in bedrock at depth *z* and time *t, and V_W (z)* is the volume of water available for

210   segregation ice growth. V_W *(z)* is estimated at each depth (z) by integrating the occurrence of unfrozen water along a path *l*,

211   starting at depth *z* and following a positive thermal gradient towards the ice lens. The volume of available water ($V_W(z)$) and

212   total flow restriction ($\Gamma(z')$), between the depth of occurrence of water (*z'*) and the location of segregation ice growth (*z*), are

213   calculated using equations 7 and 8 respectively (Andersen et al., 2015):

214   $$V_W(z) = \int_l \phi(z') w_f(z') e^{-\Gamma(z')} dz' \qquad (7)$$

215   $$\Gamma(z') = \int_z^{z'} \gamma(z'') dz'' \qquad (8)$$

216   where, l is the distance from depth *z* to the surface, lower boundary, or an interface where the thermal gradient changes signs

217   (from positive to negative or vice versa). The penalty function $e^{-\Gamma(z')}$ (Anderson et al., 2013) is a function of the total flow

218   restriction ($\Gamma(z')$) at the depth z'. Since segregation ice growth is exhibited at sub-zero temperatures (below $-3°C$) and liquid

219   water is available at positive temperatures (T $> 0°C$), water must migrate through a mixture of frozen and unfrozen soil or the

220   bedrock. The variables γ_{SW}, γ_{SC}, γ_{BW}, γ_{BC} (defined in Table 3) represent the flow restriction parameters and were used in the

221   model to approximate a range of permeabilities (Andersen et al., 2015), but do not explicitly simulate water transport.

222   The soil porosity ($\varphi_S = 0.3$) is assumed to be higher than that of bedrock ($\varphi_B = 0.02$). V_W (z) is expected to be high due to the

223   presence of unfrozen soil in the proximity of a frozen bedrock. Since Model 3 limits the positive effects of V_W to a critical

224   water volume V_{CW} (Table. 2, i.e., if $V_W > V_{CW}$, then $V_W = V_{CW}$), the expected high ($> V_{CW}$) values for V_W will not affect frost

225   cracking any further.

226   Lastly, the integrated frost cracking intensity $\acute{F}CI$ across Earth's terrestrial surface was calculated by depth integration of the

227   FCI averaged over a period of 1 year (Anderson et al., 2013):

228   $$\acute{F}CI = \frac{1}{Py} \int_0^{Py} \int_0^D FCI(z,t) dz dt \qquad (9)$$

229   where, Py is 1 year and D is the maximum depth investigated (20 m). The unit of integrated FCI in this model is $°Cm$. Integrated

230   FCI is calculated for each of the GCM simulation's model years and then averaged over the total number of years (15 years).

231

3.3. Calculation of permafrost extent

The permafrost extent in the LGM and present-day simulations were estimated using the approach of Levavasseur et al. (2011), where permafrost is assumed to be solely dependent on near surface temperatures, except in high mountainous regions with varied soil types and snow cover. The boundary conditions were adopted from (Renssen and Vandenberghe, 2003), which state that continuous permafrost exists in regions with mean annual near surface temperatures of – 8 °C or below, and coldest month temperatures of – 20 °C or lower. Furthermore, we also consider the same study's statement that discontinuous permafrost exists in the regions with MAT in the range between – 8 °C and – 4 °C.

4. Results

In the following, we document the general trends in the estimated FCI from Model 3 (Andersen et al., 2015) in all the paleoclimate time-slices (PI, MH, LGM, PLIO) based on the coupling of the above models to GCM output for these time slices. Since spatial and temporal variations in frost cracking do not vary much between the three approaches, for brevity we focus our presentation of results on the most recent (Model 3 - Andersen et al., 2015) approach, and present the results of the other two approaches (Model 1, 2; Anderson 1998 and Hales and Roering, 2007) in the supplementary material.

4.1.   Model 3: FCI as a function of thermal gradient and soil thickness

For all paleoclimate time slice experiments, the FCI predicted by Model 3 is in the range of $0 – 0.4 \ °C \ m$ at higher latitudes (30 °N – 80 °N and 20 °S – 80 °S) (Fig. 6). The maximum FCI values are observed in the higher latitudes (50 °N – 80 °N) and show the same pattern as variations in Ta when Ta exceeds 30°C.

In the PI and MH simulations, the highest FCI is observed in North America (40°N – 55°N and 70°N – 80°N) and Eurasia (35 °N – 50 °N, 55 °E – 80 °E and 55 °N – 80 °N, 80 °E – 180 °E), with values ranging from $0.08 \ °C \ m$ to $0.2 \ °C \ m$. Low FCI can be observed in South America, with values between $0.02 \ °C \ m$ and $0.05 \ °C \ m$. This is consistent with results from models 1 and 2 (see supplement).

In the LGM simulation, the highest FCI values are observed in Alaska, Turkmenistan, Uzbekistan, Eastern China and north-eastern latitudes in Eurasia (70 °N – 80 °N, 105 °E – 180 °E) with values ranging from $0.08 \ °C \ m$ to $0.22 \ °C \ m$. In the Andes of South America, the frost cracking activity is restricted to the geographical range of 12 °S – 55 °S. The highest South American FCI values (~ 0.15 °C m to ~ 0.22 °C m) are predicted for the southern part of the continent (40 °S – 50 °S). New Zealand and the western periphery of Antarctica exhibit some frost cracking activity in the LGM driven models.

Earth **Surface**
Dynamics
Discussions
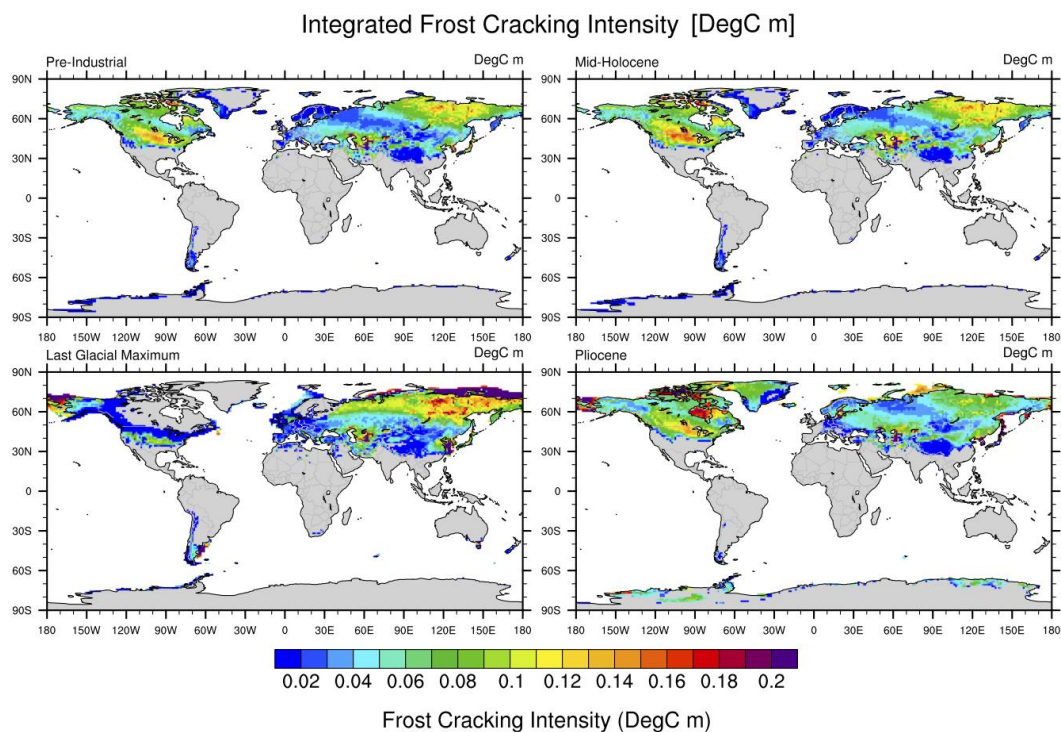
Figure 6. Model 3 predicted integrated FCI as a function of thermal gradient and sediment thickness for Pre-Industrial (top-left), Mid-Holocene (top-right), Last Glacial Maximum (bottom-left), and mid-Pliocene (bottom-right) times (unit: °C m). Data plotted in this figure are available in the supplemental material for readers interested in plotting / using it for other purposes. The grey areas in plots indicates the absence of frost cracking. For the Last Glacial Maximum time slice and Greenland and Antarctica (all time slices) the regions covered by ice were removed from the calculation and are also grey.

In the mid-Pliocene, the maximum FCI values are predicted in the higher latitudes of Canada and Alaska (0.15 °C m - 0.22 °C m). Moderately high values are predicted for Greenland (0.02 °C m – 0.12 °C m) and the northern latitudes of Eurasia (0.05 °C m – 0.16 °C m). Overall, the magnitude of mid-Pliocene FCI is lower than that of all other investigated time slices. The only exception are some high-latitude regions (NE Canada, eastern Antarctica) that exhibit locally higher FCI values in the mid-Pliocene relative to the PI. Less frost cracking activity is predicted for South America, which is consistent with the results of Model 1 (Anderson, 1998).

For all the time-slices, regions with positive MATs (0 °C to 15 °C) exhibit higher values of FCI where the sediment cover is thinner (e.g. Middle East Asia). In contrast, predictions of FCI in regions with negative MATs (-5 °C to -20 °C) and high Ta (30 °C to 40 °C) tend to be higher where sediment cover is thicker (e.g. North East Eurasia).

5. Discussion

In this section, we synthesize and interpret the results (from Model 3) at both a global and regional scales. For brevity, we limit our discussion regional variations to include Tibet, Europe and South America. For other regional areas of interest to readers, the data used in the following figures is available for download (see acknowledgements). Our presentation of selected regional

277 areas is followed by the comparison of modeled FCI with published field observations and permafrost extent in the LGM and

278 present day. We also compare the model outcomes of all the three models used in the study.

5.1. Synthesis and Interpretation

280 This section comprises the synthesis and interpretation of the trends in FCI values predicted by Model 3 for the investigated

281 paleoclimate simulations (PI, MH, LGM and PLIO). In the PI and MH simulations, high values of FCI in northern latitudes

282 (60 °N – 80 °N) in Eurasia and North America coincide with lower MATs in the range of -25 °C to -15 °C and very high Ta's

283 in the range of 30 °C to 40 °C. Furthermore, the soil thickness in some of these areas is as low as 10 – 20 cm in North America,

284 and 40 – 50 cm in Eurasia. The higher values of FCI coincide with positive MATs (~10 °C – 20 °C) in the mid-high latitudes

285 in North America, where Ta values are also high (25 °C – 30 °C) and soil cover thickness is in the range of 50 cm – 60 cm.

286 However, the highest FCI was predicted in the Middle East, which experiences similar MATs and Ta values and has

287 significantly thinner soil cover (0 cm – 20 cm). This indicates that frost cracking is more prevalent in areas with positive MATs

288 and thin or no soil cover. This confirms the findings of (Hales and Roering, 2007, 2009), and Anderson et al. ((2013),

289 2015)(2015)). FCI in areas with negative MATs and thicker soil cover (~ 80 cm – 100 cm) is mainly controlled by the Ta

290 values, due to higher Ta and high thermal gradients predicted in the subsurface, both of which facilitate ice segregation growth

291 (Hales and Roering, 2007; Hallet et al., 1991; Murton et al., 2006; Walder and Hallet, 1985). A similar effect of temperature

292 and soil thickness on frost cracking intensity is observed in the LGM and PLIO simulations.

5.2. Influence of past climate on FCI at a global scale

294 We have investigated the influence of climate change on frost cracking on different spatial scales and through geologic time

295 using 3 different frost cracking models (Anderson, 1998; Hales and Roering 2007; Andersen et al., 2015) and paleoclimate

296 GCM simulations (Mutz et al., 2018). Our results for Model 3 are presented as maps showing time-slice specific FCI anomalies

297 relative to the PI climate simulation on a global scale (Fig. 7), in Tibet (Fig. 8), Europe (Fig. 9) and South America (Fig. 10).

298 Furthermore, the spatial distribution of FCI in various climates has been compared with the glacier mask (Supplement Fig. 3)

299 where continental ice was located for all time-slices (PI, MH, LGM and PLIO). This was done to understand the reasons behind

300 the trend of FCI over time.

301 The differences in FCI between the PI and MH climate simulations are the range of – 0.04 °C m to 0.02 °C m. The MH

302 simulation yields s higher FCI values for most regions except for parts of northern Asia, mid-western Europe, mid North

303 America, Alaska, the Andes Mountains and Tibet. These differences may be attributed to the slight changes in MATs in these

304 regions.

305 The differences between PI and LGM FCI values are highest in the high latitudes (Fig. 7) in North America (ΔFCI ≈ 0.16 °C

306 m) and northern Europe (ΔFCI ≈ 0.04 °C m). This is likely due to continental glaciation in these areas (Supplement Fig. 3)

307 leading to low or no frost cracking during LGM. In the mid-high latitudes (~ 50 °N to 70 °N) of Northern Asia, LGM FCI

308 values are higher than in PI FCI values (ΔFCI ≈ - 0.06 °C m). This can be attributed to an absence of glacial cover and higher

309 Ta values (Fig. 3) in this region during the LGM. However, the LGM FCI values are higher than in the PI simulation (ΔFCI ≈

310 0.04 °C m) in the mid-high latitudes in Asia (30 °N – 50 °N), which may be attributed to the positive MATs in this area during

311 the PI simulation.

312

Earth **Surface**
Dynamics
Discussions

313
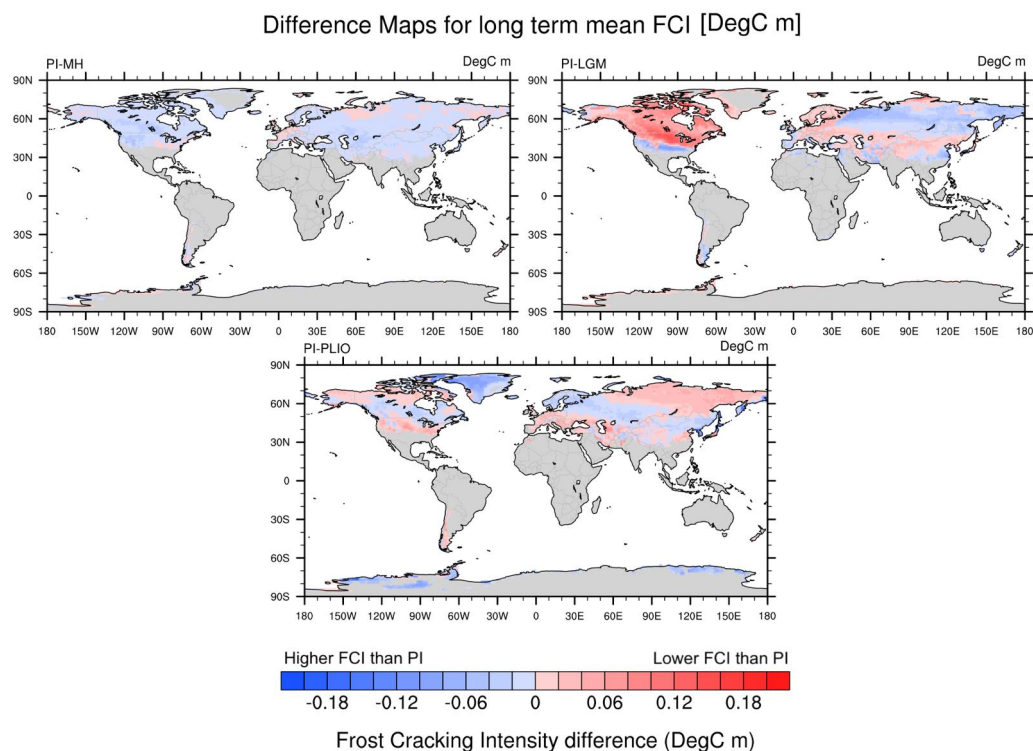
Figure 7. Differences in long-term mean FCI (Model 3) between the Pre-Industrial minus (-) the Mid-Holocene (top-left), Pre-Industrial - Last Glacial Maximum (top-right), and Pre-Industrial - mid-Pliocene (bottom) (unit: °C m) at a global scale.

The PLIO FCI (Fig. 7) is lower than PI FCI (ΔFCI ≈ 0.10 °C m) in Antarctica (150 °W – 60 °W; 100 °E – 170 °E), Greenland and in the higher latitudes of North America (70 °N – 80 °N). This may be attributed to the absence of glacial cover in these areas due to the warmer mid-Pliocene climate. The same differences can be observed in the mid-high latitudes of northern Europe, North America and Asia (40 °N – 60 °N), possibly due to higher MATs in the PLIO simulation. Higher FCI is predicted during the PI simulation in the higher latitudes in Asia (50 °N – 80 °N, 40 °E – 180 °E), Tibet, Middle East Asia, southern Europe, parts of North America (28 °N – 40 °N; 60 °N – 70 °N) and South America (the Andes Mountain range), with the FCI difference ranging from 0.02 °C m – 0.08 °C m. This can be attributed to higher Ta in the PI simulation relative to the other time slices.

In summary, the overall comparison of differences between paleo-FCI and PI-FCI indicates a low impact of changing surface temperatures between the PI and MH simulations on frost cracking. This is not surprising given the relatively small climatological differences between the simulations. The differences in FCI between PLIO and PI are more varied, but generally greater. More specifically, warmer regional climates in the Pliocene seem to facilitate frost cracking in higher latitudes, especially in Greenland, when glaciation is absent. The LGM simulation produced the greatest differences in FCI with respect to the PI simulation. These can be attributed to increased glaciation and a much colder climate in higher latitudes, including North America and Europe. High LGM-FCI values were exhibited east of the Andes Mountains in the southern part of South America, possibly due to the absence of glacial cover and high Ta values (~ 20 °C – 25 °C) (Fig. 3) in the region. The above

interpretations are in agreement with Mutz et al. (2018) and Mutz and Ehlers (2019) who suggested minor deviation of MH MATs from PI values, and high deviations in FCI in the LGM and PLIO simulations.

5.3. Regional effects of past climates on FCI
5.3.1. Tibet
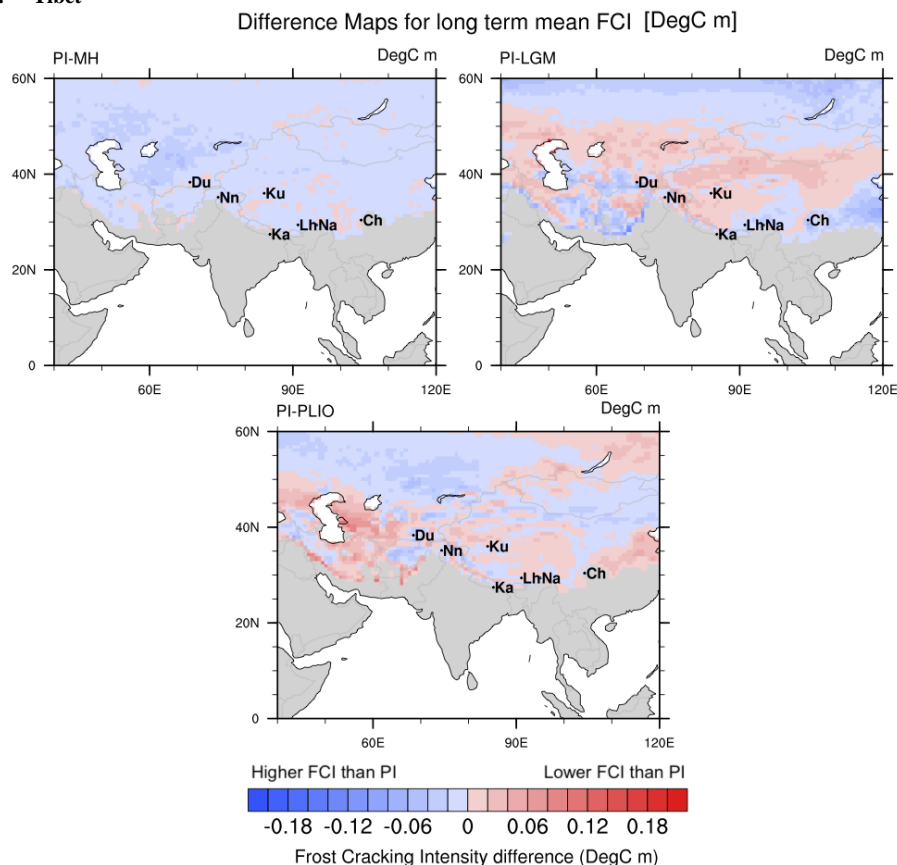
Figure 8. Differences in long-term mean FCI (Model 3) between the Pre-Industrial minus (-) the Mid-Holocene (top-left), Pre-Industrial - Last Glacial Maximum (top-right), and Pre-Industrial - mid-Pliocene (bottom) (unit: °C m) in Tibet. City abbreviations: Du – Dushambe, Nn – Srinagar, Ku – Xinjiang, Ka – Kathmandu, Lh – Lhasa, Na – Namcha Barwa, Ch – Chenshangou.

Tibet exhibits only small (~0.02 $°C\,m$), predominantly positive MH-FCI deviations from PI conditions (Fig. 8).. The PI – LGM comparison reveals higher PI FCI values (ΔFCI ≈ 0.06 $°C\,m$) on the Tibetan Plateau. Only the eastern part of Tibet, near Lhasa city, LGM FCI values are higher (ΔFCI ≈ 0.04 $°C\,m$). In the PI – PLIO comparison, the PI exhibits higher FCI values (ΔFCI ≈ 0.04 $°C\,m$) over most of the Tibetan Plateau, except for the eastern slopes of Himalayas, where PLIO-FCI values are higher (ΔFCI ≈ 0.04 $°C\,m$). The LGM simulation yields the greatest deviations from PI conditions due to significantly lower temperature and FCI values in the LGM.

5.3.2. Europe

Earth **Surface**
Dynamics
Discussions
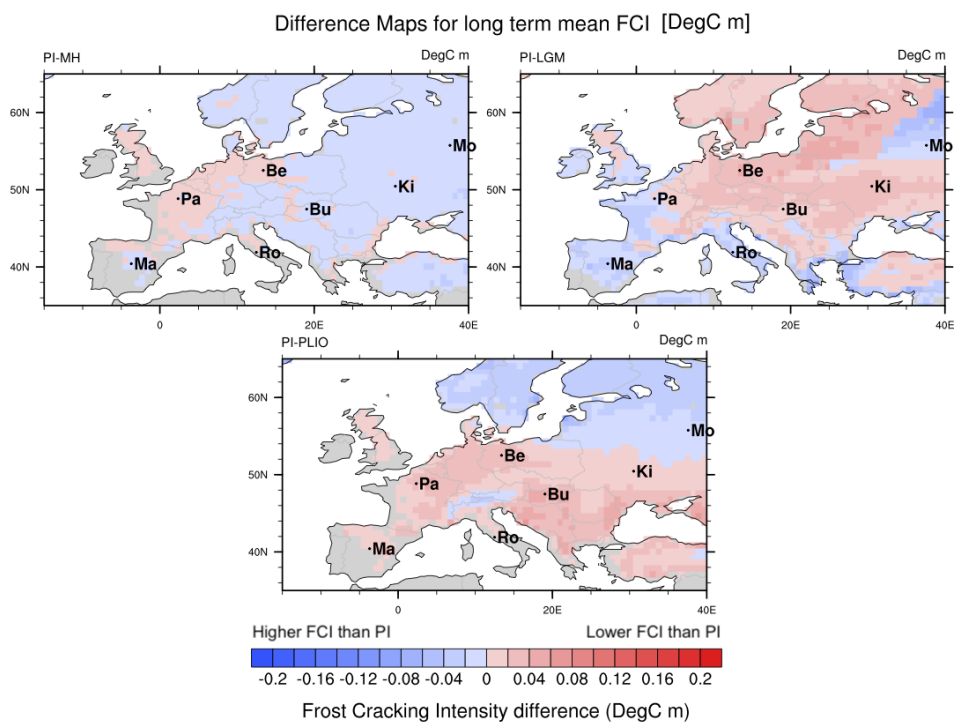
Figure 9. Differences in long-term mean FCI (Model 3) between the Pre-Industrial minus (-) the Mid-Holocene (top-left), Pre-Industrial - Last Glacial Maximum (top-right), and Pre-Industrial – the mid-Pliocene (bottom) (unit: °C m) in Europe. City abbreviations: Pa – Paris, Be – Berlin, Mo – Moscow, Ki – Kiev, Ro – Rome, Bu – Budapest, Ma – Madrid.

As in Tibet, the PI – MH comparisons for Europe (Fig. 9) reveal very small deviations in MH-FCI from PI conditions (ΔFCI ≈ -0.02 °C m to 0.02 °C m). These are negative in Western Europe (including areas near the cities of Paris, Berlin and Rome), and positive in Eastern Europe (including Budapest, Kiev and Moscow). In the PI – LGM comparison, the PI shows higher FCI (ΔFCI ≈ 0.02 °Cm – 0.06 °Cm) in central Europe (including Paris, Berlin, Budapest and Kiev), and lower FCI values (ΔFCI ≈ -0.02 °C m - -0.06 °C m) in southern Europe (including Madrid and Rome). In the PI – PLIO comparison, higher PI-FCI (ΔFCI ≈ 0.02 °C m - 0.06 °C m) is exhibited in central to southern Europe (including Madrid, Paris, Berlin, Rome, Budapest and Kiev), and lower PI-FCI prevails in northern Europe (ΔFCI≥ -0.08 °C m). Similar to Tibet, and likely for the same reasons, Europe also shows the highest impact of climate change on frost cracking during the LGM.

5.3.3.   South America

Earth **Surface**
Dynamics
Discussions
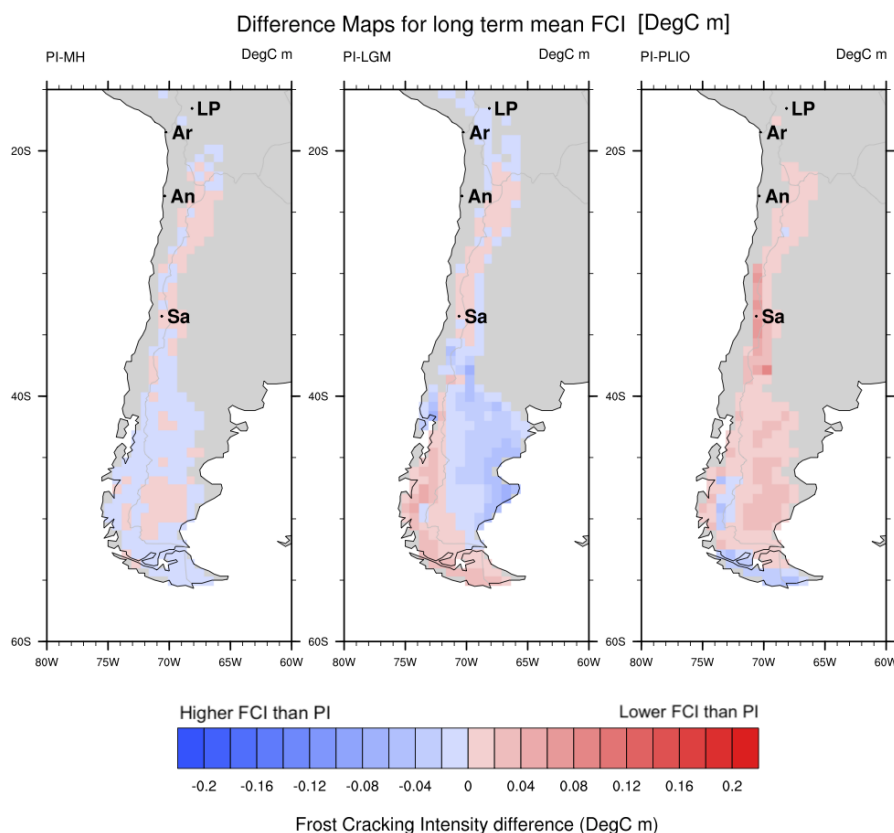
Figure 10. Differences in long-term mean FCI (Model 3) between the Pre-Industrial minus (-) the Mid-Holocene (top-left), Pre-Industrial - Last Glacial Maximum (top-right), and Pre-Industrial - mid-Pliocene (bottom) (unit: °C m) in southwestern South America. City abbreviations: LP – La Paz, Ar – Arica, An – Antofagasta, Sa – Santiago.

The magnitude of PI-MH FCI differences in southwestern South America (Fig. 10) are is similar to that of other regions (ΔFCI ≈ -0.02 °C m to 0.02 °C m). However, in the PI – LGM comparison for this region, the LGM yields lower FCI values (ΔFCI≤ 0.06 °C m) in the Andes Mountains, and the PI simulation yields lower FCI values (ΔFCI≥ -0.06 °C m) in the east of the Andes Mountains in the southern part of the region (40 °S – 50 °S). The PI – PLIO comparison reveals the highest differences in FCI (ΔFCI ≈ 0.02 °C m to 0.08 °C m). In southwestern South America, the biggest differences in frost cracking produced by the PLIO simulations, followed by the LGM simulations. This is likely caused by the temperatures in the Pliocene, which prevent the bedrock in mid-latitude South America to reach FCW.

5.4.   Comparison to observations
5.4.1.   Comparison to previous related studies

In a previous study by Amitrano et al. (2012), evidence of frost cracking in the Swiss Alps was investigated in high-alpine rock walls. The maximum values for FCI were observed in the temperature range of 0 °C to – 5 °C for granite and gneiss lithologies. The measurement site was a south facing cliff at an elevation of about ~3500 m a.s.l. with local mean annual air temperature of – 7.3 °C (1961 - 1990) and mean annual rock temperature of – 2 °C to 3 °C (Hasler et al., 2011). Amitrano et al., (2012) suggested that increased frost cracking for warmer periods could be interpreted as an effect of thermal dilation of

380 cracks. This is supported by our study, as in Model 3 results, the northern latitudes in Eurasia and mid latitudes in North

381 America and Alaska show high values of frost cracking intensity (~ 0.08 °C m – 0.18 °C m) in PI, MH and PLIO simulations.

382 Another study (Girard et al., 2013) in the Swiss Alps (Jungfraujoch) applied acoustic emission techniques and suggests

383 increased FCI for subsurface temperatures ranging from 0 °C to – 15 °C. Furthermore, Girard et al. (2013) suggested that

384 sustained freezing can yield much stronger frost cracking activity than repeated freeze-thaw cycling. Larger rates of acoustic

385 energy detected at negative temperatures (T < 0 °C) suggest that water migration and segregation ice growth play and important

386 role in frost cracking. This supports our Model 3 results for the LGM simulations in northern Eurasia and Alaska, which show

387 high FCI values in the range of ~ 0.12 °C m – 0.22 °C m.

388 Hales and Roering (2007) suggested that FCI is higher near the surface, up to a penetration depth of 4 m, because the steepest

389 thermal gradients are near to the surface. In contrast to field studies (Amitrano et al., 2012; Girard et al., 2013), Hales and

390 Roering (2007) suggested that positive MATs account for higher FCI due to the higher availability of water for segregation

391 ice growth, which is consistent with this study's high FCI in the mid-high latitudes of North America (~ 40 °N – 50 °N during

392 PI, MH and PLIO simulations and ~ 35 °N – 45 °N during LGM simulation) and mid-latitudes in South America (~ 15 °S –

393 55 °S during PI, MH and LGM simulations).

394 Anderson et al. (2013) suggested that FCI is higher for moderately low, negative MATs and that frost cracking in cold regions

395 could persist due to water transport in cold bedrock. Furthermore, Andersen et al. (2015) suggested that frost cracking can be

396 active in moderately warm climates provided that sediment cover is very thin (< 10 cm) and the surface temperature is

397 occasionally lowered into the frost cracking window. The above findings are in agreement with our computed FCI (~ 0.16 °C

398 m – 0.2 °C m) in the middle east (~ 36 °N – 48 °N and 54 °E – 80 °E), which has a relatively thin sediment cover (> 5 cm) and

399 MAT range of 5 °C to 15 °C. Finally, recent work (Marshall et al., 2015, 2017) for Western Oregon, USA, suggested that

400 periglacial processes were vigorous during the LGM, which is supported by our model showing maximum FCI values (0.12

401 °C m to 0.22 °C m) in higher latitudes in Asia (~ 70 °N – 80 °N) and Alaska (~ 60 °N – 75 °N) during LGM. Taken together,

402 the previous regional studies are consistent with the direction of change in the FCI predicted by our global analysis.

403 **5.4.2. Comparison of results to permafrost extent**

404

Earth **Surface**
Dynamics
Discussions
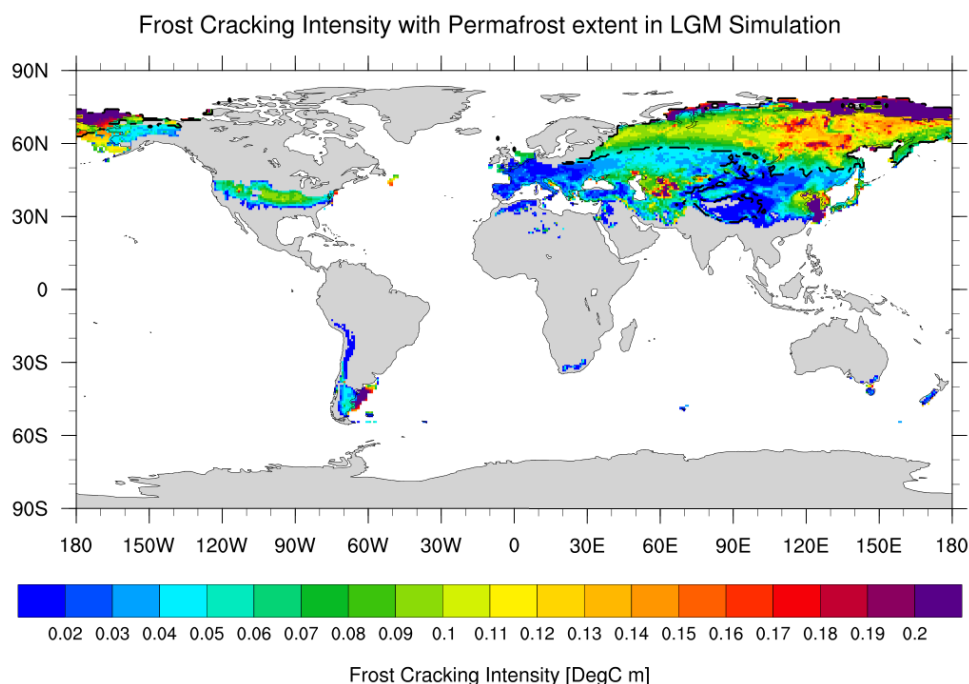
Figure 11. Frost cracking intensity (Model 3) and continuous permafrost extent in the LGM (depicted by black dashed lines).

High LGM-FCI values (> ~0.06) correlate with permafrost extent in higher latitudes in Eurasia, Alaska and Tibet and Himalayan regions (Fig. 11). Similarly, a good correlation for FCI > ~-0.06 in the PI simulation and permafrost in the PD simulation is observed for higher latitudes in Asia and North America (Fig 12). However, permafrost extent does not cover Montane and Alpine permafrost in North America near the southern extent of the ice sheet (35 °N to 45 °N latitudes) in the LGM simulation, as suggested by French and Millar (2014), where FCI exhibits a sudden increase (approx. 0.08 °C m to 0.1 °C m). Overall, FCI and permafrost extent correlate reasonably well with our predictions.
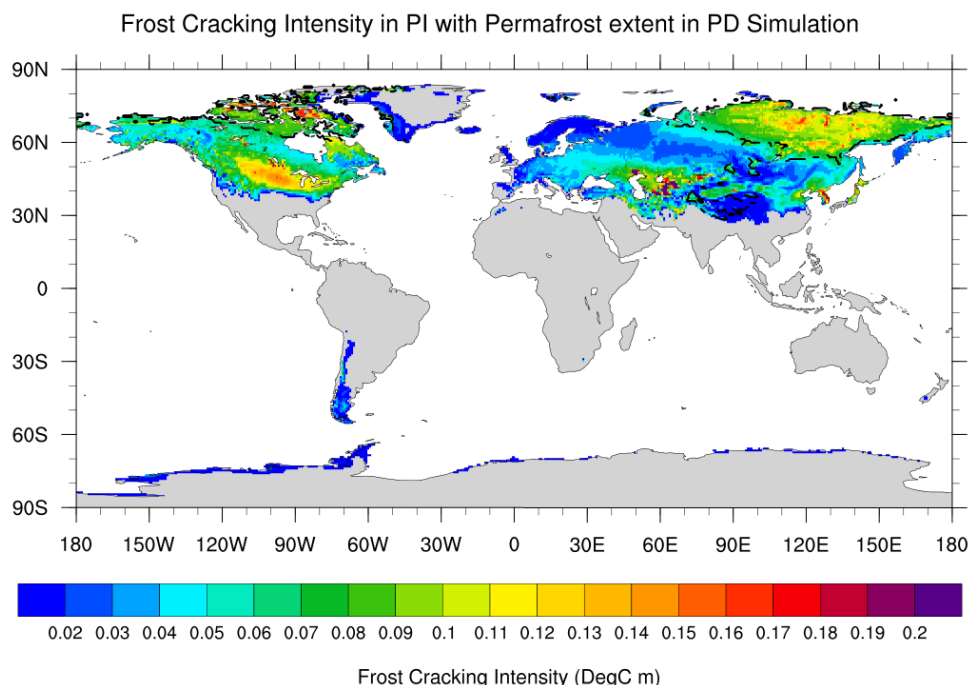
Figure 12. Frost cracking intensity in the Pre-Industrial simulation (Model 3) and continuous permafrost extent in Present-Day (depicted by black dotted line).

5.5.   Inter-comparison of Models 1-3

A comparison of the FCI predicted by the three models for the different time slices highlights some key differences (Fig. 6, and supplement Figs 1, 2). The spatial extent of frost cracking in specific time-slices is different in all the three models, which can be accredited to different inputs considered in each model, namely the availability of water for frost cracking by segregation ice growth. For example, the glaciated region (Supplement Fig. 3) in North America and Greenland exhibits the occurrence of frost cracking in Model 1, significantly reduced frost cracking in Model 2, and the complete absence of frost cracking in Model 3.

Model 1 predicts the maximum FCI values in the regions with MATs in the range of -10 °C to -5 °C, relatively low FCI values in regions with MATs of -5 °C – 0 °C, and very low values in regions characterized by high MATs above 0 °C. In contrast, Model 2 (Supplement Fig. 2) and Model 3 yield maximum FCI values for positive MATs with high Ta, as observed in previous studies (Andersen et al., 2015; Anderson et al., 2013; Hales and Roering, 2007; Marshall et al., 2015). In Model 3, the soil thickness plays an important role in the estimation of the FCI. The model produces high FCI values for areas with low soil thickness, such as < 5 cm in Eurasia (55 °E – 80 °E, 35 °N – 50 °N) and 10 cm to 20 cm for North America (50 °N – 63 °N; 70 °N – 80 °N). This result is in close agreement with Andersen et al. (2015). Due to the lower penetration depths of the freezing front, the FCI is considerably dampened in the presence of the soil cover, thereby limiting the bedrock from reaching FCW in cases of positive MATs (Andersen et al., 2015).

The spatial pattern of frost cracking in Model 3 is influenced by consideration of segregation ice growth, in which the available volume of water (V_W) in the vicinity of an ice lens is critical. Segregation ice growth and sediment cover are responsible for

434 the observed patterns in FCI. The other models considered (see supplement Fig. 1, 2) do not explicitly account for both these
435 processes and therefore produce different predictions of the FCI in some regions.

436

437 **5.6.   Model Limitations**

438 Here we discuss the limitations of the 3 frost cracking models and uncertainties stemming from the application of the ECHAM5
439 simulations as input to these models. One of the most important limitations is the use of the same soil thickness for each of
440 our paleoclimate time-slices (Wieder, 2014). In reality, the soil thickness may be different for PI, MH, LGM, and PLIO due
441 to erosion and sedimentation. However, there are currently no other global estimates of paleo soil thickness available.
442 Therefore, using present-day thickness remains the best-informed and feasible approach. Furthermore, uniform thermal
443 diffusivity and porosity were used for bedrock and sediment cover over the globe for simplification, even though thermal
444 diffusivity and porosity vary for different Earth materials. The application of different thermal diffusivities for individual
445 lithologies was not considered, although typical thermoconductivity variations of rocks can vary by a factor of 2-3 at the most
446 (Ehlers, 2005). In addition, our models neglect the hydrogeological properties of bedrock, including moisture content and
447 permeability for calculation of subsurface temperature variations, which may influence water availability for frost cracking.
448 To the best of our knowledge, there are no global inventories of these properties that are suited for studies such as ours. In our
449 approach, we assume that these material properties are spatially and temporally constant. As a result, our predictions are only
450 suited as adequate representations of greater regional trends in FCI, and the reader is advised that local deviations from our
451 values are likely and depend on near surface geologic and hydrologic variations. A further source of uncertainties stems from
452 possible inaccuracies in paleoclimate estimates that drive the frost cracking models. The reader is referred to Mutz et al. (2018)
453 for further discussion of the GCM's limitations. Given the above limitations, we cautiously highlight that the results presented
454 here are essentially maps of FCI sensitivity to climate change forcing. Although broad agreement is found between our
455 predictions and previous work (Section 5.5), we caution that geologic and hydrologic complexities in the 'real world' may
456 produce variations in FCI driven by hydrologic and geologic heterogeneities we are unable to account for.

457 Finally, it is worth noting that only selected time slices were evaluated here. Although the LGM was a significant global glacial
458 event, previous (and more extreme) ice ages occurred in the Quaternary. Therefore, the spatial patterns of FCI predicted here
459 may not match observations in all areas, particularly where they have a 'periglacial hangover' of frost cracking from previous
460 glaciations.

461 **6.   Conclusions**

462 We presented three approaches to quantify the frost cracking intensity (FCI) for different times in the Late Cenozoic, namely
463 pre-industrial (PI, ~1850 CE), Mid-Holocene (MH, ~6 ka), Las Glacial Maximum (LGM, ~21 ka) and mid-Pliocene (PLIO,
464 ~3 Ma). These approaches are based on process-informed frost cracking models and their coupling to paleoclimate simulations
465 (Mutz et al., 2018). A simple one-dimensional heat conduction model (Hales and Roering, 2007) was applied along with FCI
466 estimation approaches from Anderson (1998) and Anderson et al. ((2013)(1998)). Our analysis and presentation of results
467 focused on the most recent and more thoroughly parameterized approach of Andersen et al., (2015; Model 3). Specifically, we
468 quantified the change in direction and magnitude of FCI in the above-mentioned climate states with respect to the PI control
469 simulation. The major findings of our study include:

470   1.   The latitudinal extent of frost cracking in the PI and MH are very similar, in Eurasia (28 °N – 80 °N), North America
471   (40 °N – 80 °N) and South America (20 °S – 55 °S). During the LGM, the FCI extent is reduced in Eurasia (28 °N –
472   78 °N) and North America (35 °N – 75 °N), and increased in South America (15 °S – 55 °S). This can be attributed

473   to extensive glaciation in the northern parts of Canada, Greenland and Northern Europe not favoring the frost cracking

474   process. In the PLIO, the FCI extent is similar to that of PI in Eurasia (30 °N – 80 °N) and North America (40 °N –

475   85 °N). PLIO-FCI values are higher in Canada (~ 0.16 $°C\,m$ to 0.18 $°C\,m$) and Greenland (~ 0.08 $°C\,m$), but

476   significantly reduced in South America (21 °S – 55 °S) with values of FCI below 0.02 $°C\,m$.

477   2. MH climatic conditions induce only small deviations of FCI from PI values, whereas the colder (LGM) and warmer

478   (PLIO) climates produce larger FCI anomalies, which are consistent with the findings of Mutz and Ehlers, 2019.

479   3. Higher frost cracking intensities in the PI simulation spatially correlate with the occurrence of continuous permafrost

480   in the PD at higher latitudes in Eurasia and North America. On the other hand, during the LGM, high frost cracking

481   in Alaska and northern latitudes of Eurasia show a good correlation with continuous predicted permafrost of the same

482   time.

483   The predicted changes in FCI presented here do not entirely confirm our hypothesis that: Late Cenozoic global climate change

484   resulted in varying intensity in FCI such that more intense frost cracking at lower latitudes during colder climates. Of particular

485   interest is that although we document latitudinally influenced spatial and temporal changes in FCI, these changes are not

486   uniform at the same latitude. The largest changes in FCI between time slices occur in different geographic regions at different

487   time periods meaning that a more simplified approach of assuming only latitudinal shifts in FCI between cold and warm

488   periods is not sufficient and that spatial changes in global climate need to be taken into account.

489   Finally, we suggest that Model 3 can be adapted in future work to regional conditions, using field geological and

490   hydrogeological parameters for better accuracy (Andersen et al., 2015). The results of this study can further be used in

491   modelling the erosion and denudation processes related to frost cracking. Predictions for potential future sites that are prone

492   to hazards related to frost cracking, such as rockfall, can be generated by coupling these models to climate simulations forced

493   with different greenhouse gas concentration scenarios representing different possible climate conditions of the future.

494   **Code availability**

495   The code and data used in this study are freely available upon request.

496   **Author contributions**

497   HS, SM and TAE designed the initial model setup and simulation programs and conducted model modifications, simulation

498   runs and analysis. HS and TAE prepared the manuscript with contributions from SM.

499   **Competing interests**

500   The authors declare that they have no competing interests.

501   **Acknowledgements:**

502   H.S, S.G.M. and T.A.E. acknowledge support by Open Access Publishing Fund of University of Tübingen. We thank XX and

503   YY for constructive reviews. The primary model results from this study (Model 3) are available in the supplemental material

504   for plotting / use by interested readers. The climate model results used in this study are available via information provided in

505   Mutz et al., (2018). H.S and T.A.E. acknowledge support from the Research Training Group 1829 Integrated Hydrosystem

506   Modelling, funded by the German Research Foundation (DFG). In addition, T.A.E, acknowledges support from the German

507   priority research program *EarthShape: Earth Surface Shaping by Biota* (SPP-1803; grant EH329/14-2), and support from the

508   California Institute of Technology Moore Distinguished Scholar program.

References

510   Abe-Ouchi, A., Saito, F., Kageyama, M., Braconnot, P., Harrison, S.P., Lambeck, K., Otto-Bliesner, B. L., Peltier, W. R.,

511   Tarasov, L.,Peterschmitt, J.-Y., and Takahashi, K.: Ice-sheet configuration in the CMIP5/PMIP3 Last Glacial Maximum

512   experiments, Geosci. Model Dev., 8, 3621–3637, https://doi.org/10.5194/gmd-8-3621-2015, 2015.

513   Acosta, V. T., Schildgen, T. F., Clarke, B. A., Scherler, D., Bookhagen, B., Wittmann, H., von Blanckenburg, F., and Strecker,

514   M. R.: Effect of vegetation cover on millennial-scale landscape denudation rates in East Africa, 7, 408–420,

515   https://doi.org/10.1130/L402.1, 2015.

516   Adams, B. A., Whipple, K. X., Forte, A. M., Heimsath, A. M., and Hodges, K. V.: Climate controls on erosion in tectonically

517   active landscapes, 6, eaaz3166, https://doi.org/10.1126/sciadv.aaz3166, 2020.

518   Amitrano, D., Gruber, S., and Girard, L.: Evidence of frost-cracking inferred from acoustic emissions in a high-alpine rock-

519   wall, Earth and Planetary Science Letters, 341–344, 86–93, https://doi.org/10.1016/j.epsl.2012.06.014, 2012.

520   Andersen, J. L., Egholm, D. L., Knudsen, M. F., Jansen, J. D., and Nielsen, S. B.: The periglacial engine of mountain erosion

521   - Part 1: Rates of frost cracking and frost creep, Earth Surf. Dynam., 3, 447–462, https://doi.org/10.5194/esurf-3-447-2015,

522   2015.

523   Anderson, R. S.: Near-surface Thermal Profiles in Alpine Bedrock: Implications for the Frost Weathering of Rock, Arctic and

524   Alpine Research, 30, 362–372, https://doi.org/10.1080/00040851.1998.12002911, 1998.

525   Anderson, R. S., Anderson, S. P., and Tucker, G. E.: Rock damage and regolith transport by frost: an example of climate

526   modulation of the geomorphology of the critical zone: ROCK DAMAGE AND REGOLITH TRANSPORT BY FROST, Earth

527   Surf. Process. Landforms, 38, 299–316, https://doi.org/10.1002/esp.3330, 2013.

528   Botsyun, S., Ehlers, T. A., Mutz, S. G., Methner, K., Krsnik, E., and Mulch, A.: Opportunities and Challenges for

529   Paleoaltimetry in "Small" Orogens: Insights From the European Alps, Geophysical Research Letters, 47, e2019GL086046,

530   https://doi.org/10.1029/2019GL086046, 2020.

531   Davidson, G. P. and Nye, J. F.: A photoelastic study of ice pressure in rock cracks, Cold Regions Science and Technology, 11,

532   141–153, https://doi.org/10.1016/0165-232X(85)90013-8, 1985.

533   Delunel, R., van der Beek, P. A., Carcaillet, J., Bourlès, D. L., and Valla, P. G.: Frost-cracking control on catchment denudation

534   rates: Insights from in situ produced 10Be concentrations in stream sediments (Ecrins–Pelvoux massif, French Western Alps),

535   Earth and Planetary Science Letters, 293, 72–83, https://doi.org/10.1016/j.epsl.2010.02.020, 2010.

536   Egholm, D. L., Andersen, J. L., Knudsen, M. F., Jansen, J. D., and Nielsen, S. B.: The periglacial engine of mountain erosion

537   - Part 2: Modelling large-scale landscape evolution, Earth Surf. Dynam., 3, 463–482, https://doi.org/10.5194/esurf-3-463-

538   2015, 2015.

539   Ehlers, T. A. and Poulsen, C. J.: Influence of Andean uplift on climate and paleoaltimetry estimates, Earth and Planetary

540   Science Letters, 281, 238–248, https://doi.org/10.1016/j.epsl.2009.02.026, 2009.

541   Eppelbaum, T. A., Kutasov, I., and Pilchin, A.: Thermal Properties of Rocks and Density of Fluids, in: Applied Geothermics,
542   Springer-Verlag Berlin Heidelberg, 99–149, 2014.

543   French, H. M. and Millar, S. W. S.: Permafrost at the time of the Last Glacial Maximum (LGM) in North America, Boreas,
544   43, 667–677, https://doi.org/10.1111/bor.12036, 2014.

545   Girard, L., Gruber, S., Weber, S., and Beutel, J.: Environmental controls of frost cracking revealed through in situ acoustic
546   emission measurements in steep bedrock: IN SITU MEASUREMENTS OF FROST CRACKING, Geophys. Res. Lett., 40,
547   1748–1753, https://doi.org/10.1002/grl.50384, 2013.

548   Hales, T. C. and Roering, J. J.: Climatic controls on frost cracking and implications for the evolution of bedrock landscapes,
549   J. Geophys. Res., 112, F02033, https://doi.org/10.1029/2006JF000616, 2007.

550   Hales, T. C. and Roering, J. J.: A frost "buzzsaw" mechanism for erosion of the eastern Southern Alps, New Zealand,
551   Geomorphology, 107, 241–253, https://doi.org/10.1016/j.geomorph.2008.12.012, 2009.

552   Hallet, B., Walder, J. S., and Stubbs, C. W.: Weathering by segregation ice growth in microcracks at sustained subzero
553   temperatures: Verification from an experimental study using acoustic emissions, Permafrost Periglac. Process., 2, 283–300,
554   https://doi.org/10.1002/ppp.3430020404, 1991.

555   Hasler, A., Gruber, S., and Haeberli, W.: Temperature variability and offset in steep alpine rock and ice faces, The Cryosphere,
556   5, 977–988, https://doi.org/10.5194/tc-5-977-2011, 2011.

557   Herman, F. and Champagnac, J.-D.: Plio-Pleistocene increase of erosion rates in mountain belts in response to climate change,
558   Terra Nova, 28, 2–10, https://doi.org/10.1111/ter.12186, 2016.

559   Kellerer-Pirklbauer, A.: Potential weathering by freeze-thaw action in alpine rocks in the European Alps during a nine year
560   monitoring period, Geomorphology, 296, 113–131, https://doi.org/10.1016/j.geomorph.2017.08.020, 2017.

561   Levavasseur, G., Vrac, M., Roche, D. M., Paillard, D., Martin, A., and Vandenberghe, J.: Present and LGM permafrost from
562   climate simulations: contribution of statistical downscaling, Clim. Past, 7, 1225–1246, https://doi.org/10.5194/cp-7-1225-
563   2011, 2011.

564   Marshall, J. A., Roering, J. J., Bartlein, P. J., Gavin, D. G., Granger, D. E., Rempel, A. W., Praskievicz, S. J., and Hales, T.
565   C.: Frost for the trees: Did climate increase erosion in unglaciated landscapes during the late Pleistocene?, Sci. Adv., 1,
566   e1500715, https://doi.org/10.1126/sciadv.1500715, 2015.

567   Marshall, J. A., Roering, J. J., Gavin, D. G., and Granger, D. E.: Late Quaternary climatic controls on erosion rates and
568   geomorphic processes in western Oregon, USA, Geological Society of America Bulletin, 129, 715–731,
569   https://doi.org/10.1130/B31509.1, 2017.

570   Matsuoka, N.: Direct observation of frost wedging in alpine bedrock, Earth Surf. Process. Landforms, 26, 601–614,
571   https://doi.org/10.1002/esp.208, 2001.

572   Matsuoka, N.: Frost weathering and rockwall erosion in the southeastern Swiss Alps: Long-term (1994–2006) observations,
573   Geomorphology, 99, 353–368, https://doi.org/10.1016/j.geomorph.2007.11.013, 2008.

574 Messenzehl, K., Meyer, H., Otto, J.-C., Hoffmann, T., and Dikau, R.: Regional-scale controls on the spatial activity of rockfalls
575 (Turtmann Valley, Swiss Alps) — A multivariate modeling approach, Geomorphology, 287, 29–45,
576 https://doi.org/10.1016/j.geomorph.2016.01.008, 2017.

577 Murton, J. B., Peterson, R., and Ozouf, J.-C.: Bedrock Fracture by Ice Segregation in Cold Regions, Science, 314, 1127–1129,
578 https://doi.org/10.1126/science.1132127, 2006.

579 Mutz, S. G. and Ehlers, T. A.: Detection and explanation of spatiotemporal patterns in Late Cenozoic palaeoclimate change
580 relevant to Earth surface processes, Earth Surf. Dynam., 7, 663–679, https://doi.org/10.5194/esurf-7-663-2019, 2019.

581 Mutz, S. G., Ehlers, T. A., Werner, M., Lohmann, G., Stepanek, C., and Li, J.: Where is Late Cenozoic climate change most
582 likely to impact denudation?, Cross-cutting themes: Impacts of climate change on Earth surface dynamics,
583 https://doi.org/10.5194/esurf-2017-47, 2018.

584 Peizhen, Z., Molnar, P., and Downs, W. R.: Increased sedimentation rates and grain sizes 2±4 Myr ago due to the in¯uence of
585 climate change on erosion rates, 410, 7, 2001.

586 Rangwala, I. and Miller, J. R.: Climate change in mountains: a review of elevation-dependent warming and its possible causes,
587 Climatic Change, 114, 527–547, https://doi.org/10.1007/s10584-012-0419-3, 2012.

588 Raymo, M. E. and Ruddiman, W. F.: Tectonic forcing of late Cenozoic climate, Nature, 359, 117–122,
589 https://doi.org/10.1038/359117a0, 1992.

590 Rempel, A. W., Marshall, J. A., and Roering, J. J.: Modeling relative frost weathering rates at geomorphic scales, Earth and
591 Planetary Science Letters, 453, 87–95, https://doi.org/10.1016/j.epsl.2016.08.019, 2016.

592 Renssen, H. and Vandenberghe, J.: Investigation of the relationship between permafrost distribution in NW Europe and
593 extensive winter sea-ice cover in the North Atlantic Ocean during the cold phases of the Last Glaciation, Quaternary Science
594 Reviews, 22, 209–223, https://doi.org/10.1016/S0277-3791(02)00190-7, 2003.

595 Rode, M., Schnepfleitner, H., and Sass, O.: Simulation of moisture content in alpine rockwalls during freeze-thaw events:
596 Simulation of Moisture Content in Alpine Rock Walls, Earth Surf. Process. Landforms, 41, 1937–1950,
597 https://doi.org/10.1002/esp.3961, 2016.

598 Roeckner, E., Bäuml, G., Bonaventura, L., Brokopf, R., Esch, M., Giorgetta, M., Hagemann, S., Kirchner, I., Kornblueh, L.,
599 Manzini, E., Rhodin, A., Schlese, U., Schulzweida, U., and Tompkins, A.: The atmospheric general circulation model ECHAM
600 5. PART I: Model description, Max Planck Institute for Meteorology, Hamburg, Germany, 2003.

601 Savi, S., Delunel, R., and Schlunegger, F.: Efficiency of frost-cracking processes through space and time: An example from
602 the eastern Italian Alps, Geomorphology, 232, 248–260, https://doi.org/10.1016/j.geomorph.2015.01.009, 2015.

603 Simmons, A. J., Burridge, D. M., Jarraud, M., Girard, C., and Wergen, W.: The ECMWF medium-range prediction models
604 development of the numerical formulations and the impact of increased resolution, Meteorl. Atmos. Phys., 40, 28–60,
605 https://doi.org/10.1007/BF01027467, 1989.

606 Turcotte, D. and Schubert, G.: Geodynamics, 3rd ed., Cambridge University Press,
607 https://doi.org/10.1017/CBO9780511843877, 2014.

608 Walder, J. S. and Hallet, B.: A theoretical model of the fracture of rock during freezing, GSA Bulletin, 96, 336–346,

609 https://doi.org/10.1130/0016-7606(1985)96<336:ATMOTF>2.0.CO;2, 1985.

610 Wieder, W.: Regridded Harmonized World Soil Database v1.2, https://doi.org/10.3334/ornldaac/1247, 2014.

611 Wei, W. and Lohmann, G.: Simulated Atlantic Multidecadal Oscillation during the Holocene, J. Climate, 25(20), 6989–7002,

612 doi:10.1175/JCLI-D-11-00667.1, 2012.

613 Werner, C., Schmid, M., Ehlers, T. A., Fuentes-Espoz, J. P., Steinkamp, J., Forrest, M., Liakka, J., Maldonado, A., and Hickler,

614 T.: Effect of changing vegetation and precipitation on denudation – Part 1: Predicted vegetation composition and cover over

615 the last 21 thousand years along the Coastal Cordillera of Chile, 6, 829–858, https://doi.org/10.5194/esurf-6-829-2018, 2018.

616 Whipple, K. X.: The influence of climate on the tectonic evolution of mountain belts, Nature Geosci, 2, 97–104,

617 https://doi.org/10/fjpxxz, 2009.

618 Wieder, W.: Regridded Harmonized World Soil Database v1.2, https://doi.org/10.3334/ornldaac/1247, 2014.